



**Environmental  
Science**  
Water Research & Technology

**The Diversity of Aluminum-Based Drinking Water Treatment Residuals for Use in Environmental Remediation**

Journal:	<i>Environmental Science: Water Research &amp; Technology</i>
Manuscript ID	EW-ART-05-2022-000387.R1
Article Type:	Paper

SCHOLARONE™  
Manuscripts

**Water Impact Statement:**

We are reporting novel data about the chemical characterization of drinking water treatment residuals (DWTRs) in the perspective of understanding what controls their high metal sorption capacities. We show that these properties are related to the selection of additives beyond the coagulant. This research informs the potential application of DWTRs for the remediation of polluted sites.

Cite this: DOI: 00.0000/xxxxxxxxxx

## The Diversity of Aluminum-Based Drinking Water Treatment Residuals for Use in Environmental Remediation<sup>†</sup>

Samuel M. Wallace,<sup>a</sup> Yuchi Zhang,<sup>a</sup> Lang Zhou,<sup>b</sup> Qing Ma,<sup>c</sup> William E. Guise,<sup>c</sup> Nancy D. Denslow,<sup>d</sup> Jean-Claude Bonzongo,<sup>b</sup> and Jean-François Gaillard<sup>\*a</sup>

Received Date

Accepted Date

DOI: 00.0000/xxxxxxxxxx

Drinking water treatment residuals (DWTRs) are complex mixtures of organic and inorganic phases generally disposed of as waste materials. However, their strong sorptive properties could be further exploited to immobilize contaminants. To characterize these materials, we applied a range of analytical techniques to a set of aluminum-based DWTRs. We determined surface areas, elemental compositions using CHNS analysis and X-ray fluorescence (XRF), performed thermogravimetric analyses paired with mass spectrometry (TGA-MS), and used synchrotron-based methods: X-ray diffraction (XRD) and X-ray absorption spectroscopy (XAS). Elemental analyses and specific surface area measurements – that vary between  $7.23 \pm 0.03$  and  $197.6 \pm 0.9 \text{ m}^2/\text{g}$  – indicate that non-coagulant additives must play an important role in controlling sorption. High resolution powder XRD reveals the presence of only a few crystalline minerals mostly derived from source waters or additives. Fe was detected by XRF in all samples, whereas Mn was present in significant levels in samples with potassium permanganate as additive. The chemical speciation of these elements was characterized by performing spectral decompositions of XAS spectra. The spectral features of Fe are consistent with iron(III) oxides/hydroxides and structural iron in clays. On the other hand, Mn is predominantly present under its reduced form, Mn(II).

### 1 Introduction

Drinking water treatment residuals (DWTRs) are the byproducts of the coagulation, flocculation, and sedimentation steps of conventional drinking water treatment<sup>1</sup>. At these stages, turbidity is removed from source waters using coagulants (such as alum,  $\text{Al}_2(\text{SO}_4)_3$ , or ferric chloride,  $\text{FeCl}_3$ ) and often flocculation aids (such as polyacrylamide and Poly-diallyldimethylammonium chloride – polyDADMAC – polymers)<sup>2</sup>. In addition, other chemicals may be added to alter the composition of incoming waters at this time; for example, lime ( $\text{CaO}$  or  $\text{Ca}(\text{OH})_2$ ), potassium permanganate ( $\text{KMnO}_4$ )<sup>2</sup>, and activated carbon. What results is a complex organic-inorganic mixed material that includes components from both the source water and the chemical additives used at the drinking water treatment plant<sup>1</sup>.

Management and disposal of DWTRs can place a significant cost burden on municipalities<sup>3</sup>. In conventional drinking water treatment, DWTRs are generated at a volumetric ratio of 1:300-500 to treated water; the relative volume of DWTRs increases by an order of magnitude at drinking water treatment plants (DWTPs) that employ lime softening<sup>3</sup>. In the United States, DWTRs are sometimes directly discharged into the environment upon their generation when permitted by state or regional authorities through the National Pollutant Discharge Elimination System (NPDES)<sup>3</sup>. In other situations, more rigorous steps may be necessary to dispose of DWTRs. For example, DWTRs may be dewatered and applied to land, or they may be disposed of as sludge in sewers to be managed by wastewater treatment plants through “indirect discharge”<sup>3</sup>. Hazardous DWTRs, as often determined through toxicity characteristic leaching procedure (TCLP) results, may need to be disposed of at hazardous waste landfills or through the use of Class I well injections<sup>4</sup>. Even among non-hazardous DWTRs, there are historic and lingering concerns about their environmental impacts, including the potential release of aluminum in acidic environments<sup>5</sup>, issues due to compromised DWTP source waters<sup>6</sup>, potential adverse ecosystem impacts<sup>7,8</sup>, and the use of synthetic organic polymers to aid flocculation<sup>9</sup>. It is worth emphasizing that most studies have found limited to negligible environmental and health impacts from the

<sup>a</sup> Department of Civil and Environmental Engineering, Northwestern University, 2145 Sheridan Road, Evanston, IL 60208, USA. E-mail: jf.gaillard@northwestern.edu

<sup>b</sup> Engineering School of Sustainable Infrastructure and Environment, Department of Environmental Engineering Sciences, University of Florida, PO Box 116450, Gainesville, FL 32611, USA.

<sup>c</sup> DND-CAT Synchrotron Research Center, Northwestern University, 9700 South Cass Avenue, Argonne, IL 60439, USA.

<sup>d</sup> Departments of Physiological Sciences and of Biochemistry and Molecular Biology and Center for Environmental and Human Toxicology, University of Florida, University of Florida, Gainesville, FL 32610, USA.

<sup>†</sup> Electronic Supplementary Information (ESI) available.

disposal of these DWTRs, provided reasonable precautions are taken<sup>5,8</sup>.

Recent research has sought to find ways to repurpose DWTRs as sorbent materials<sup>1,10</sup>. Indeed, DWTRs are characterized by high sorption capacities for arsenic<sup>11,12</sup>, inorganic phosphorus<sup>13,14</sup>, and mercury<sup>15,16</sup>. However, these studies may be somewhat limited in scope, since they tend to focus on a specific DWTR characterized by the coagulant of choice. This leaves the richness in the diversity of these materials generally under-addressed. Hence, there is a need to characterize the chemical diversity of DWTRs that derive from the use of the same coagulant to gain insights into what controls sorptive properties.

Here, we characterize DWTR samples obtained from 6 DWTPs in the United States. Each of these samples comes from treatment plants that use an aluminum-based coagulant. These samples, however, differ in terms of the other chemical additives used as well as the water sources (*e.g.* surface water, groundwater, or a mix of the two). For this, we apply a multi-method approach that relies on (1.) thermogravimetric analysis coupled to mass spectroscopy (TGA-MS) for broad quantification of material composition, (2.) specific surface area analysis and microporosity relying on the BET theory, (3.) elemental composition by means of x-ray fluorescence (XRF) and CHNS analyses, and (4.) the characterization of crystalline and amorphous mineral phases by high-resolution X-ray diffraction (XRD) and X-ray absorption spectroscopy (XAS).

## 2 Experimental

### 2.1 Drinking Water Treatment Residual (DWTR) Samples

Drinking water treatment residuals were obtained from DWTPs across the United States. State of origin, chemical additives, and type of source water (surface or groundwater) for each sample are included in Table 1. These DWTRs were selected from a total of 15 samples after a screening step based on metal content guidelines for safe introduction of waste materials to aquatic environments<sup>7,17</sup>. Each DWTR sample is referred by the abbreviation of the state of origin – for example, DWTR-TN refers to the sample from Tennessee. Dewatered DWTR samples provided by DWTPs were air-dried and subsequently ground. For each DWTR, particles of less than 2 mm in size were separated from the bulk DWTRs using a No. 10 mesh, producing the fine material used in all experiments.

All DWTRs analyzed in this study use an aluminum salt as part of the coagulation process. That aluminum salt is aluminum sulfate ( $\text{Al}_2(\text{SO}_4)_3$ , or “alum”), with the exception of DWTR-TN, which uses polyaluminum chlorohydrate (PACl,  $\text{Al}_n\text{Cl}_{3n-m}(\text{OH})_m$ ). Aluminum coagulants form aluminum hydroxide,  $\text{Al}(\text{OH})_3$  that decreases the alkalinity of the solution, but PACl partially offsets this through its basicity.

Beyond the coagulant, all but the MN sample use synthetic organic polymers to aid in flocculation. NC, OR, and WY use anionic polymers (which are generally polyacrylamide polymers), while UT and TN use cationic polymers (which are generally poly-DADMAC polymers). These are applied at low-to-sub-ppm levels to source waters to lessen the necessary coagulant dose<sup>2</sup>.

Half of the samples (MN, NC, and TN) employ lime softening, where  $\text{CaO}$  or  $\text{Ca}(\text{OH})_2$  is added to the source waters to remove Mg and Ca from solution through precipitation<sup>2</sup>.

Potassium permanganate ( $\text{KMnO}_4$ ) is used to oxidize unwanted chemicals in source waters, such as sulfide, organic matter, ferrous iron, and reduced manganese<sup>2</sup>. UT and TN use  $\text{KMnO}_4$  as an additive. Other chemicals may be used for similar oxidative purposes, but these additives will not themselves form a precipitate as a result. Within the suite of DWTRs, these include chlorine gas (OR), ozone (WY), and hydrogen peroxide (TN, again).

Finally, UT and WY samples use activated carbon as an additive, which sorbs dissolved contaminants in the source waters.

Most of these DWTRs come from treatment plants that draw primarily (as in WY and MN) or exclusively (as in OR, TN, and UT) from surface waters. DWTR-NC is the exception: all the water for that treatment plant comes from groundwater wells.

### 2.2 Thermogravimetric Mass Spectrometry (TGA-MS)

Thermogravimetric analysis data were collected using a Netzsch STA 449 F3 Jupiter Simultaneous Thermal Analysis (STA) instrument. Measurements were made under ultra-high purity helium gas flowing at 211 mL/min. Following a 10-minute isothermal step at 30°C, the temperature was increased at a rate of 10°C/min up to 900°C and held at that temperature in a final isothermal step for 10 minutes. Gases were transferred to an Agilent Technologies 7890A Gas Chromatograph equipped with an Agilent HP-5 column and Agilent 5975 MSD spectrometer. Injections of 250  $\mu\text{L}$  of the gas mixtures were analyzed every minute through the heating and final isothermal steps, and mass spectra were collected from 10–400 m/z. A baseline measurement using an empty alumina crucible under the same operating conditions was collected to correct for the buoyancy effect. Approximately 15 mg of the fine fractions for each DWTR were used for this analysis. Mass losses for the DWTRs are expressed relative to the mass at the end of the initial isothermal step. Samples were dried at 40 °C for one day prior to analysis.

Mass spectrometry (MS) data were analyzed using Agilent ChemStation software. For quantification of the major ions at m/z 18 (water) and 44 (carbon dioxide), integration of the peaks were performed within the software. For the peak forest maps showing the m/z ranging from 50 to 150, raw data were exported. The median count value for each m/z was calculated starting at 5 minutes after the commencement of the high-temperature isothermal step and ending at the last collected MS data point approximately 20 minutes later during the declining temperature step. This median value provided the baseline to estimate the integrated peak area for the high m/z ions.

### 2.3 Specific Surface Area and Microporosity Analysis by Nitrogen Adsorption

Surface area analysis was conducted on the fine fraction of DWTR samples based on the physisorption of nitrogen using a Micromeritics 3Flex instrument. DWTRs were dried at 40 °C, then immediately prior to analysis, samples were degassed at 100 and 120°C using a Micromeritics Smart VacPrep. Samples were con-

Table 1 DWTR sample characteristics, including their state of origin, chemical additives used in drinking water treatment, and general source waters.

State	Additives	Water Source
MN	Aluminum sulfate, lime, ferric chloride	70 – 80% surface water, remainder groundwater
NC	Aluminum sulfate, lime, anionic polymer	Groundwater
OR	Aluminum sulfate, chlorine gas, anionic polyacrylamide polymer, sodium hydroxide	Surface water
TN	Polyaluminum chlorohydrate, potassium permanganate, lime, soda ash, hydrogen peroxide, cationic polymer	Surface water
UT	Aluminum sulfate, potassium permanganate, activated carbon, cationic polymer	Surface water
WY	Aluminum sulfate, anionic polyacrylamide polymer, powdered activated carbon, sodium fluorosilicate, ozone	Mostly surface water with some groundwater supplementation

firmed to be ready for analysis if their leak rate was less than 0.0025 mmHg/min after 120 s.

Surface area calculations are based on the Brunauer-Emmett-Teller (BET) theory<sup>18</sup>, while pore size distributions are based on the Barrett-Joyner-Halenda (BJH)<sup>19</sup> method with the Halsey *t*-curve<sup>20</sup> as applied to desorption data.

#### 2.4 Carbon, Hydrogen, Nitrogen, and Sulfur Elemental Analysis (CHNS)

Data for the elemental abundance for carbon, hydrogen, nitrogen, and sulfur (CHNS) in DWTR samples were collected using the Elementar Vario EL Cube. Sulfanilamide standards were used to verify the accuracy of the measurements. For each DWTR, triplicate measurements were taken using approximately 5 mg of sample for each measurement.

Measurements were taken for DWTR samples with and without the addition of phosphoric acid. Acidification allows for the contribution of acid-volatile carbon to be distinguished from non-acid volatile forms of carbon; most often, the acid-volatile carbon is dominated by carbonate minerals, and the non-acid-volatile carbon would primarily be made up of organic matter<sup>21</sup>. Two DWTR samples, UT and WY, are sourced from DWTPs that use activated carbon as an additive; importantly, activated carbon is also non-acid-volatile. 50 mg of each sample was placed in a glass vial and dried at 40 degrees Celsius for one day. For acidified samples, 1.5 M H<sub>3</sub>PO<sub>4</sub> was added in a 50 μL initial spike. Subsequent additions of acid were applied in 100 μL increments. Samples were dried at 60°C after each addition of acid. A total of 50 μL acid was added to OR and WY, 150 μL to UT, and 750 μL to TN, NC, and MN. These volumes were selected to ensure a molar ratio of protons from the acid to carbonate of at least 6:1<sup>21</sup> based on the estimated carbonate content for each DWTR as suggested by chemical additives used and the TGA data collected.

After all acid was added, these samples were dried for three days at 40° C. Mass of these samples were tracked across time and corrected using an empty sample bottle undergoing the same heat treatment. H, N, S, and total C abundance values were taken from the results of un-acidified samples. The non-acid-volatile C was taken from the acidified samples (corrected based on the change in mass with the addition of acid), and the acid-volatile C abundance was taken to be the difference between C measurements in the two samples.

#### 2.5 X-Ray Fluorescence (XRF)

XRF data were collected using a Xenometrix Ex-Calibur EX-2600. This instrument uses a Rh X-ray source, operated here at 20 keV and 10 μA, and a silicon energy-dispersive detector. Spectra were collected for 120 s with no filter over the detector. All samples used the fine fraction of the DWTRs with data collected at room temperature under vacuum. Samples were placed on 6 μm Mylar film stretched over plastic cups.

#### 2.6 X-Ray Diffraction (XRD)

Powder XRD measurements were first performed using laboratory based diffractometers. However it proved difficult to resolve the presence of other crystalline phases than quartz and calcite. Hence, synchrotron-based high-resolution powder XRD analyses were conducted at the bending magnet beamline of the Dow-Northwestern-Dupont Collaborative Access Team (DND-CAT), Sector 5 of the Advanced Photon Source at Argonne National Laboratory in Lemont, IL, USA. Fine and ground samples were sieved through a 63 μm 230 mesh. These were subsequently sealed in glass capillaries that were rotated within the monochromatic X-ray beam, which had a wavelength  $\lambda = 0.620426 \text{ \AA}$ , which translates to an energy of 20 keV. The scan ran from  $2\theta$  values of 7.5 to 41.5°. Peak identification was performed using MDI-JADE software<sup>22</sup> with the International Centre for Diffraction Data database<sup>23</sup>, and additional crystallographic information was collected from the American Mineralogist Crystal Structure Database<sup>24</sup>.

#### 2.7 X-Ray Absorption Spectroscopy (XAS)

Like the XRD analyses, XAS data were collected at DND-CAT on the bending magnet beamline. Data for samples were collected at the Fe and Mn K-edges in fluorescence mode using two Vortex ME-4 silicon drift detectors and aligned in energy using a reference foil for the metal of interest. For standard/reference materials, data were collected in absorbance mode. Intensities for *I*<sub>0</sub>, *I*<sub>T1</sub>, and *I*<sub>T2</sub> were measured with Oxford ionization chambers of 29.6 cm path lengths, and energy was set using a Si (111) double crystal monochromator. Other Fe K-edge standards were collected from previous XAS experiments<sup>25</sup>, the Lawrence Berkeley National Laboratory XAS database<sup>26</sup>, and the National Institute for Materials Sciences Materials Data Repository (MDR)<sup>27,28</sup>. Mn database standards include spectra from previous studies<sup>29</sup>, dis-

tributed with the Demeter suite for XAFS analysis<sup>30</sup>, found on the MDR<sup>27,28</sup>, and included in supplementary materials by Manceau, Marcus, and Grangeon<sup>31</sup>. For standards without reference foil data included, a spectrum from the database was aligned to data collected at DND-CAT (either Mn or Fe metal foil or manganese carbonate), and the offset for the alignment was applied to all the spectra from that database.

XAS data analysis was performed using araucaria<sup>32</sup>, a data analysis package written in Python and utilizing Jupyter notebooks<sup>33</sup>. This software package depends on scipy<sup>34</sup>, sklearn<sup>35</sup>, and numpy<sup>36</sup>. Glitches were removed from the spectra automatically<sup>37</sup>. For the interpretation of X-ray absorption near edge spectra (XANES), principal component analysis (PCA) and target transformation performed on the spectral libraries of references (TT) were performed to inform about the selection of the proper set spectra to use. This was followed by performing spectral decompositions based on linear combination fitting (LCF)<sup>38–40</sup>. These techniques were applied to the first-derivative XANES for spectra at both the Mn and Fe K-edge<sup>25</sup>.

Calculations for the LCF were performed using lmfit<sup>41</sup>, forcing the sum of standards to be equal to 1. Standards were eliminated from the LCF for each sample if (1.) the uncertainty for that standard's weight in the fit encompassed 0 or (2.) the omission of that standard from the LCF resulted in an increase of  $<0.001$  in the  $\chi^2$  measure for goodness-of-fit.

### 3 Results and Discussion

We present below the results of the suite of analyses that were performed to characterize air-dried and ground DWTR samples. As a preamble, one needs to note that exposing reduced elements, such as Fe(II) or Mn(II), to di-oxygen may lead to their oxidation and therefore changes in their coordination environment/speciation. At the same time, since we did not control the chain of custody of the samples that were shipped to us and that their application would occur after storage and transport, most likely as dried granulate, air-drying seemed to be the most effective and sustainable approach for the re-use of stabilized DWTRs.

#### 3.1 Thermogravimetric Mass Spectrometry

Thermogravimetric results are presented in Figure 1. These data divide the DWTRs neatly into two groups: those with relatively consistent declines in mass from 100–600°C, and those which see steep declines in mass above 600°C. This division corresponds with the use of lime as an additive. Above 600°C, carbonate minerals decompose, releasing carbon dioxide<sup>42</sup>; the high mass loss in that region is tied to high carbonate mineral content in lime-based DWTRs (MN, NC, TN). Mass loss in other regions is broadly indicative of the organic matter and water content of these materials. Below 200°C, most mass loss will be connected to the dehydration of the materials<sup>42</sup>. Between 200 and 600°C, several decomposition processes may contribute to mass loss. Distinguishing organic matter decomposition in this region by TGA remains a point of research interest; in general, though quantification of inorganic carbon in carbonate minerals is quite accurate based

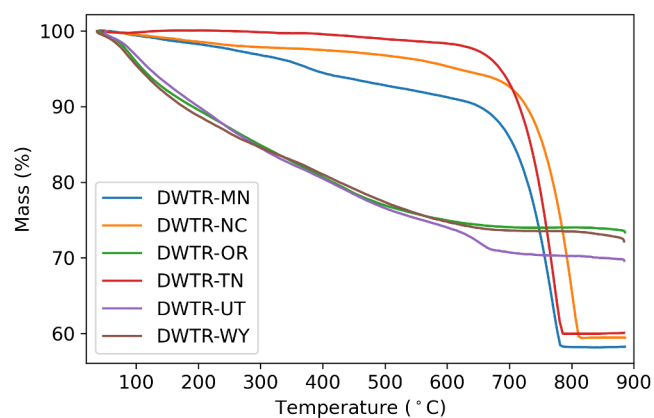


Fig. 1 Thermogravimetric results for DWTR samples. Mass of the DWTR, shown as the percentage of the mass relative to the mass at the end of the initial isothermal step, is compared to temperature.

Table 2 Thermogravimetric analysis results for DWTR samples, showing the percentage mass loss over specified temperature ranges. Mass loss from (1.) 200–430°C may be attributed to organic matter decomposition, (2.) 430–600°C inorganic material decomposition, and (3.) 600–825°C carbonate mineral decomposition<sup>42</sup>.

DWTR Samples		Mass Loss (%)		
		200–430°C	430–600°C	600–825°C
Lime-based	NC	1.3	2.0	35.9
	MN	4.4	2.7	33.1
	TN	0.7	1.1	38.4
No lime	OR	10.1	4.5	1.0
	UT	10.8	5.2	3.9
	WY	8.9	5.1	1.4

on the mass loss above 500<sup>43</sup> or 600°C<sup>42</sup>, attempts to quantify organic carbon can lead to less accurate, but still informative, results<sup>43,44</sup>. Broadly speaking, in soils, mass loss from 200–430°C<sup>42</sup> or similar temperature ranges<sup>43</sup> has been attributed to the decomposition of organic matter. From 430–600°C, non-carbonate mineral decomposition (i.e. clays) can factor into the mass loss<sup>42</sup>. However, these are imperfect assumptions. Magnesium hydroxide, which is assumed to precipitate during the lime softening process<sup>2</sup>, will lose a significant amount of mass within that “organic matter” range<sup>45</sup>. Organic matter can decompose across the full range of temperatures, depending on its composition, and under an inert atmosphere, decomposition can be incomplete<sup>42</sup> (an inert atmosphere was used to minimize the decomposition of activated carbon<sup>46,47</sup>, allowing some separation between organic and activated carbon not feasible through analyses like CHNS). Despite these complicating factors, the TGA provides a starting point for characterizing the material. Mass losses in these regions are presented in Table 2.

DWTRs without lime lose approximately 10% of their mass in the “organic” region for TGA; by comparison, NC and TN samples lose much less, approximately 1%. MN is intermediate to these extremes, but because magnesium hydroxide decomposes in a similar region, further evidence through mass spectrometry

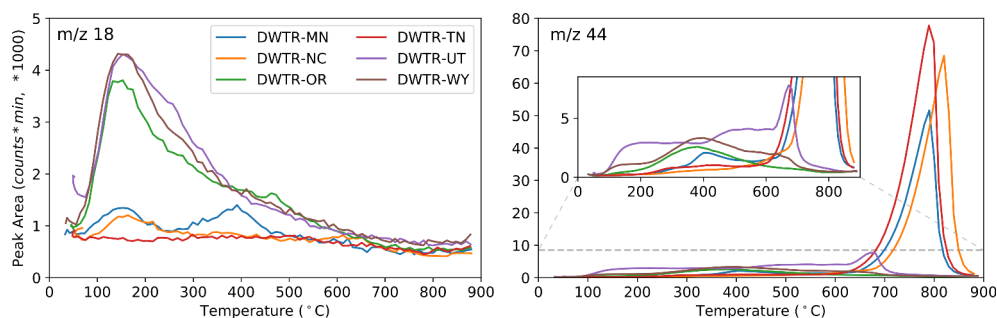
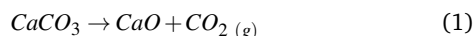


Fig. 2 Peak areas as a function of temperature for  $m/z$  18 (water, left subplot) and 44 (carbon dioxide, right subplot) from the mass spectra collected from the TGA-MS. Note the difference in y-axis scales for these two subplots: carbon dioxide reaches much larger peak areas (nearly 80,000  $\text{counts} \cdot \text{min}$ ), specifically above 600°C in lime-based DWTRs. The inset in the bottom subplot zooms in to provide detail at lower temperatures and in non-lime-based DWTRs.

and elemental analysis will be needed to assert that MN has more organic matter than its lime-based peers.

Figure 2 shows the peak areas of two mass-to-charge ratios from the mass spectra of the gases released from the DWTRs as a function of temperature: water ( $m/z$  18) and carbon dioxide ( $m/z$  44). The steep release of carbon dioxide in lime-based DWTRs (and, to a lesser extent, DWTR-UT) further validate the connection between mass loss above 600°C and carbonate decomposition. Through this, the inorganic carbon from carbonate minerals can be approximated for these samples. Assuming all mass loss in that region is due to the release of carbon dioxide, carbon from carbonates will make up less than 0.5% of the mass in OR and WY samples; 1.1% of the UT sample; and range from 9.0% (MN) to 10.5% (TN) in the lime-based DWTRs. Provided that all this inorganic carbon is in the form of calcium carbonate, lime-based DWTRs are found by Equation 1 to range from 75% (MN) to 87% (TN) calcium carbonate. Particularly at 87% calcium carbonate, these findings align with the order-of-magnitude increase in waste volume at lime softening drinking water treatment plants<sup>3</sup>.



The peak areas in the lower temperature ranges show that the phases contributing to mass loss here are less clear-cut. DWTRs OR, WY, and MN have distinct peaks in the release of carbon dioxide near 400°C, which would suggest the significance of the decomposition of organic matter near that temperature. However, that carbon dioxide release tails off well above the 430°C informal threshold between organic matter and inorganic decomposition. The peak for water near 400°C in the MN sample also doesn't discount the dehydration of magnesium hydroxide driving some change in mass for that sample. Moreover, UT sees relatively consistent release of carbon dioxide from 100-600°C. A better understanding of these processes may be achieved by tracking the release of higher  $m/z$  ions attributable to organic matter, though more precise quantification will demand elemental analysis.

The mass spectra as a function of temperature for higher  $m/z$  values, ranging from 50 to 150, are shown in Figure 3. Lime-based DWTRs MN, NC, and TN show low intensity and low diversity in the peaks here. MN, and to a lesser extent, NC, show

some high-temperature release of an ion at  $m/z$  64, which could be attributable to the decomposition of sulfates and the release of  $\text{SO}_2$ <sup>48</sup>. DWTRs without lime (OR, UT, and WY) show much higher intensity and diversity in their mass spectra at this  $m/z$  range. These ions span the 200-600°C range, suggesting both that the 200-430°C range will underestimate organic matter and 200-600°C would capture most organic matter decomposition, at the risk of including other processes.

### 3.2 Specific Surface Area and Microporosity Analysis by Nitrogen Adsorption

BET surface area results are presented in Figure 4 along with pore size distributions. Specific surface areas of the samples tested vary between 7.23 to 197.6  $\text{m}^2/\text{g}$  for TN and UT samples, respectively. UT has a much higher surface area than any of the other DWTRs, and this is attributable to the high microporosity observed in that sample. These characteristics are most likely due to the use of activated carbon as an additive for the UT sample. WY also contains activated carbon as an additive, but that limited fraction does not lead to a similarly high surface area or microporosity. Among the lime-based DWTRs, MN and TN both have relatively low calculated surface areas. NC is the exception, using lime as an additive and possessing the second-highest BET surface area among all samples. With the exception of the UT sample, microporosity is limited in these DWTRs, which are more accurately characterized as mesoporous.

### 3.3 Elemental Analyses

#### 3.3.1 CHNS.

CHNS results are presented in Figure 6, with each element plotted as its percentage mass in the DWTR in Subplot A. The lime-based DWTRs have a very high quantity of acid-volatile carbon; the quantities here are well-aligned with the those estimated from TGA-MS, with findings through CHNS of  $9.34 \pm 0.09\%$  acid-volatile carbon in MN,  $9.58 \pm 0.05\%$  in NC, and  $10.4 \pm 0.1\%$  in TN (compared with 9.0, 9.8, and 10.5% carbonate carbon, respectively, by TGA-MS). In contrast, the non-lime-based DWTRs tend to have very high standard deviations for measurements of inorganic carbon relative to the mean findings. WY had especially large variance in measurements of both acid-volatile and

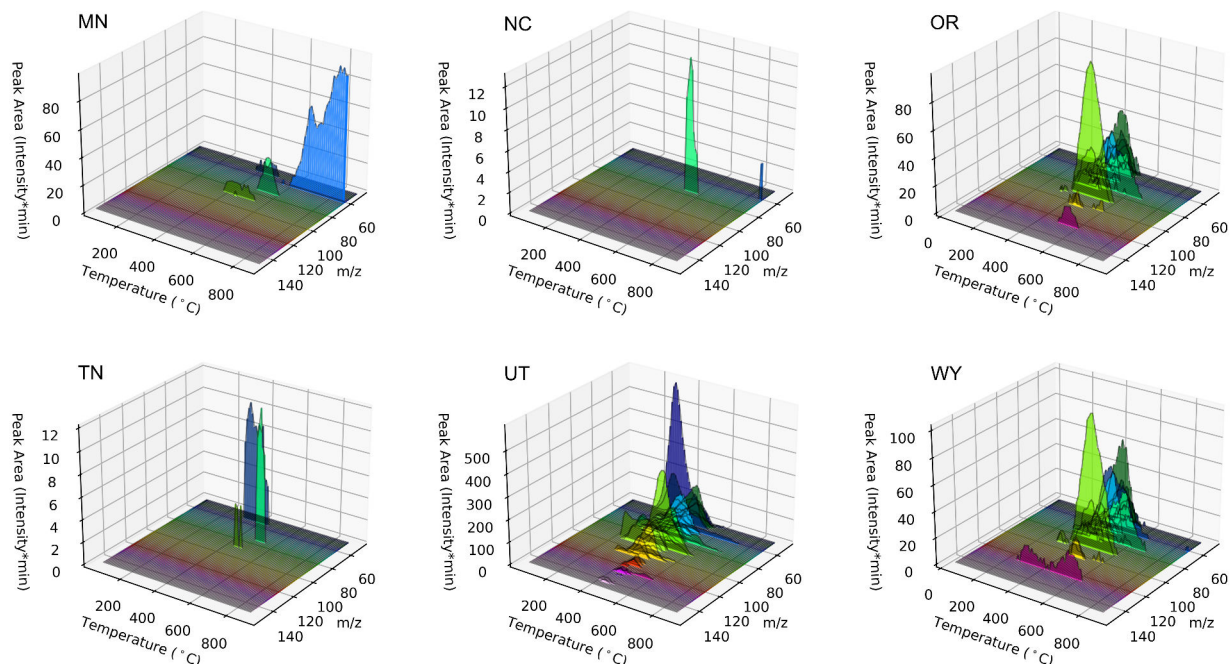


Fig. 3 Peak forests showing the area corresponding to each ions across the temperature range for TGA-MS analysis. Results are shown for  $50 < m/z < 150$  during the rising temperature portion of the experiment. Note the differences in the scales for the peak areas recorded. The peak forests here show a clear division between lime- and non-lime-based DWTRs. Lime-based DWTRs (MN, NC, TN) show relatively low peak areas and diversity in this range, while non-lime-based DWTRs (OR, UT, WY) show intense, diverse peaks, particularly between 300-600°C, but also spreading into lower and higher temperature ranges.

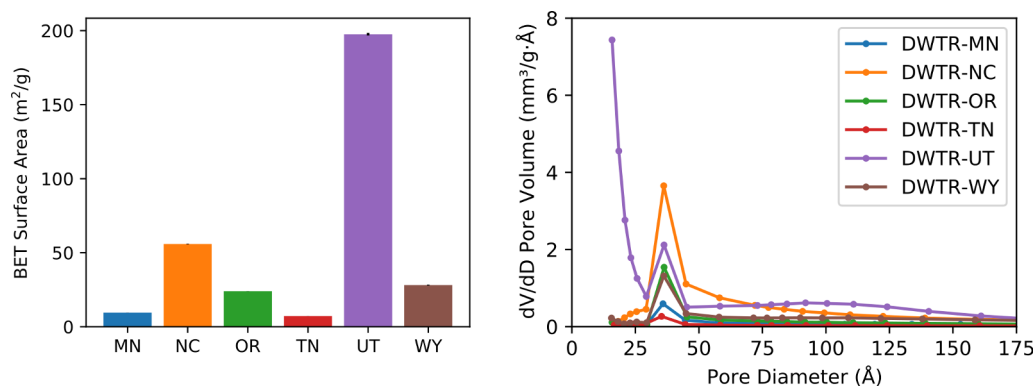


Fig. 4 BET surface area results for the six DWTR samples. Calculated surface areas, along with the uncertainties of the fit to the BET model, are displayed in the left subplot. Pore volume distribution for DWTRs as a function of pore diameter are shown in the right subplot. Results were calculated using desorption data with the BJH method<sup>19</sup>. The UT sample shows an especially large pore volume in the micropore region, which drives its large BET surface area. For the other samples, the surface area is largely attributable to mesoporosity.

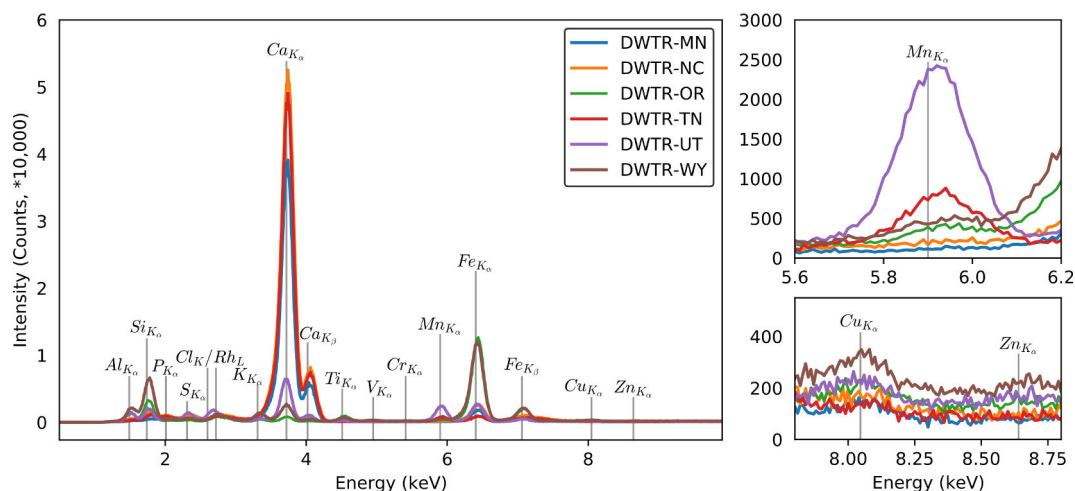


Fig. 5 X-ray fluorescence spectra for drinking water treatment residual samples. Spectra were collected at 20 keV and 10  $\mu$ A with no filter and are not normalized. The left subplot shows the full spectrum for each sample; peaks are immediately discernible down to the  $Al_{K\alpha}$  fluorescence line and up to the  $Fe_{K\beta}$  fluorescence line. The top right subplot focuses on the  $Mn_{K\alpha}$  fluorescence line. MN and TN have distinct, well-defined peaks here. Signals for OR and WY are also slightly elevated, though the fluorescence here overlaps with what is detected for the high  $Fe_{K\alpha}$  peaks. Finally, the bottom right subplot focuses on  $Cu_{K\alpha}$  and  $Zn_{K\alpha}$  emission lines. Peaks here are poorly defined and very low intensity across all DWTR samples.

non-acid-volatile C not seen in H, N, or S measurements. This indicates heterogeneity specific to carbon measurements, which may be attributable to some non-uniformity in the distribution of the activated carbon additive for WY.

The non-acid-volatile carbon measurements follow a general pattern where they are least abundant in lime-based DWTRs, more abundant in OR and WY, and most abundant in UT. The non-acid-volatile C is generally attributable to organic carbon<sup>21</sup>, but it also will include activated carbon in both the UT and WY samples. These results confirmed what was observed previously by the determination of the specific surface area, *i.e.*, the large fraction of non-acid-volatile C in the UT sample compared to any of the other samples is likely due to a large addition of activated carbon. Within the lime-based DWTRs, MN has nearly double the non-acid-volatile C content ( $1.86 \pm 0.09\%$ ) compared to the next-highest sample ( $1.0 \pm 0.1\%$  for TN).

Subplot B of Figure 6 shows the molar fraction of N and S in the DWTRs. As before, lime-based DWTRs show significantly lower concentrations of these elements than non-lime-based DWTRs. In the group without lime, some of the effects from before are slightly tempered without the influence of activated carbon. UT, which has the highest non-acid-volatile C fraction, also has the highest quantities of N and S; WY, which clearly had the second-most non-acid-volatile C, is on par with OR in terms of concentration for N and S. In the lime group, MN has the greatest quantity of N and S combined – a notable finding, considering MN is the only DWTR in this set that does not include a synthetic organic polymer. NC has a disproportionately high concentration of S along with a very low concentration of N. It is also the only DWTR sample to be drawn exclusively from groundwater. Given the sizable fraction of more reducing conditions in aquifers of the region<sup>49</sup>, this could be reflective of a small, but still impactful fraction of sulfide minerals pulled up from the aquifer. The CHNS findings for the UT sample along with the division be-

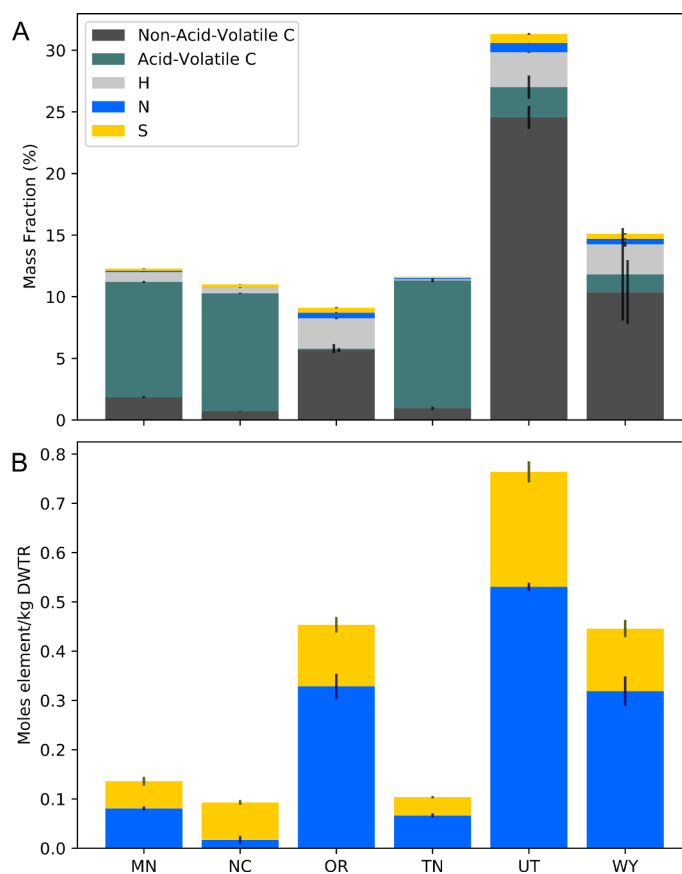


Fig. 6 CHNS elemental analysis results for DWTR samples. Subplot A shows the mass fractions of hydrogen, nitrogen, sulfur, and acid-volatile and non-acid-volatile carbon in terms of the percent mass of the DWTR. Subplot B shows the moles of nitrogen and sulfur per kg DWTR.

tween DWTRs with and without lime highlight the contribution of chemical additives to DWTR composition; however, the MN and NC sample results show that the influence of source water chemistry, particularly on these elements, cannot be discounted.

### 3.3.2 X-Ray Fluorescence.

To detect for the presence of dominant elements in DWTR samples, we used XRF. Results are presented in Figure 5. Fluorescent yield ( $\omega$ ) increases with increasing atomic number<sup>50</sup>; as such, despite the relatively high expected concentrations of Al from the coagulants, the limited fluorescent yield of x-rays by this element limits the intensity of the peaks. It is also worth emphasizing that direct comparisons of the peak size for different samples only provide limited meaning. Factors, including the thickness of the sample, will impact the intensities of the XRF spectra. However, relative comparisons of elemental abundance are possible. For example, WY has a peak for iron that is larger than its peak for Ca, while NC has a peak for Ca that is larger than its peak for Fe. Ergo, NC will have a greater ratio of Ca to Fe compared to WY, and vice versa.

DWTRs that use lime as an additive (NC, MN, TN) are dominated by an intense signal at 3.7 keV corresponding to the  $\text{Ca}_{K\alpha}$  fluorescence lines<sup>50</sup>. All DWTRs showed some peak there; of the DWTRs without a lime additive, only UT had its largest peak at the  $\text{Ca}_{K\alpha}$  line, though relative to the other elements seen in the UT spectrum, this line was less intense than NC, MN, and TN samples.

At lower energies, the distinct peak for Cl in the UT sample (overlapping with the Rh source peak) implies a relatively high salt content in that particular DWTR. This is unsurprising, given the desert environment of Utah, but it does highlight the caution needed prior to utilizing these materials for environmental remediation in freshwater environments<sup>7</sup>.

Of the elements suitable for XAS analysis at the bending magnet beamline of the Sector 5 of the Advanced Photon Source, only Mn and Fe are present in sufficient quantities to provide a sizable fluorescent signal. Like Ca, all samples show a discernible peak at the  $\text{Fe}_{K\alpha}$  line, with WY and OR showing particularly strong fluorescence. On the other hand, UT and TN show the largest signals for Mn. Unsurprisingly, these are the two DWTR samples that include  $\text{KMnO}_4$  as an additive. OR and WY samples have slightly elevated intensities in the region of the  $\text{Mn}_{K\alpha}$  line, but these are strongly influenced by the intense  $\text{Fe}_{K\alpha}$  fluorescence. For other trace elements that may be suitable for XAS analysis, including Cu and Zn, peaks were indistinct and of low intensity. Based on these results, XAS data were collected at the Fe K-edge for all DWTR samples and at the Mn K-edge for UT and TN samples.

### 3.4 X-Ray Diffraction

In contrast to laboratory-source powder XRD†, high-resolution XRD produces a diffraction pattern with especially well-resolved peaks and practically no background signal due to the use of monochromatic X-rays. As a result, it is particularly well suited to determine crystallite size if any peak can be detected from background<sup>51</sup>. Hence, it greatly eases mineral identification. The high-resolution XRD patterns for the six DWTR samples are

shown in Figure 7. Lime-based DWTRs (MN, NC, and TN) showed high-intensity diffraction patterns corresponding to calcite, suggesting an abundance of highly crystalline calcite. In terms of carbonate minerals, low-intensity peaks for calcite and dolomite were also present in the UT diffraction pattern, whereas in the WY sample, only dolomite was detected. Quartz tends to be ubiquitous in many DWTRs and was identified in the diffraction patterns of TN, UT, OR, and WY. Finally, patterns corresponding to feldspar (albite and microcline) and clay (illite or smectite) were observed in OR and WY samples at low intensities.

Aside from the presence of calcite, which is ubiquitous in the lime-based DWTRs, all crystalline phases identified correspond to minerals that would originate from the source waters rather than the ones that can be generated by the addition of aluminum salts or chemical additives. In fact, each of the identified crystalline phases is commonly found in XRD patterns of sediments<sup>52</sup>. Crystalline aluminum and iron hydroxides were not detected, and no crystalline manganese minerals can be detected in the UT and TN samples which use  $\text{KMnO}_4$  as an additive.

Hence these results suggest that the aluminium salts and the chemical additives applied at DWTPs lead initially to the formation of amorphous precipitates. These amorphous phases can however transform into more crystalline precipitates upon ageing, *e.g.* Ostwald ripening, as was suggested in the case of the addition of Al salts to lake sediments in order to limit phosphorus efflux<sup>53,54</sup>. Alternatively, one can promote the formation of more crystalline phases, *e.g.* gibbsite in the case of aluminum hydroxide, by heating the DWTR<sup>55</sup> in order to increase P sorption.

Consequently, we turned our attention to a method that probes short range order, x-ray absorption spectroscopy, to investigate the amorphous nature of the solid phases present in DWTRs that can play a significant role in sorption processes. This can be primarily done by looking at the Fe and Mn K-edges.

## 3.5 X-Ray Absorption Spectroscopy

### 3.5.1 Fe K-edge XAS.

First-derivative XANES data at the Fe K-edge and LCF results are presented in Figure 8. Target transformations based on the first derivative of the spectra performed after principal component analysis are presented in Fig. A5 of the SI†. Most of the samples are quite similar with one exception: the spectrum of the MN sample shows very distinct features. There is a pronounced shoulder above 7130 eV and oscillations near 7140 eV. One should note that the MN DWTR is the only one that contains  $\text{FeCl}_3$  as an additive, which is applied in storage lakes prior to intake for the DWTP. Aside from this, NC and TN samples are quite similar, while UT, WY, and OR samples also cluster together. Yet again, clear divisions in material properties emerge between lime-based and non-lime-based DWTRs.

Using standard spectra for illite<sup>26</sup> and hydrous ferric oxide (HFO), the non-lime-based DWTRs can be reconstructed with a high degree of confidence. Illite was selected as a standard due to its observed presence in XRD for OR and WY samples. These results indicate iron is in predominantly ferric form for non-lime-based DWTRs, but a significant fraction of this iron may be tied to

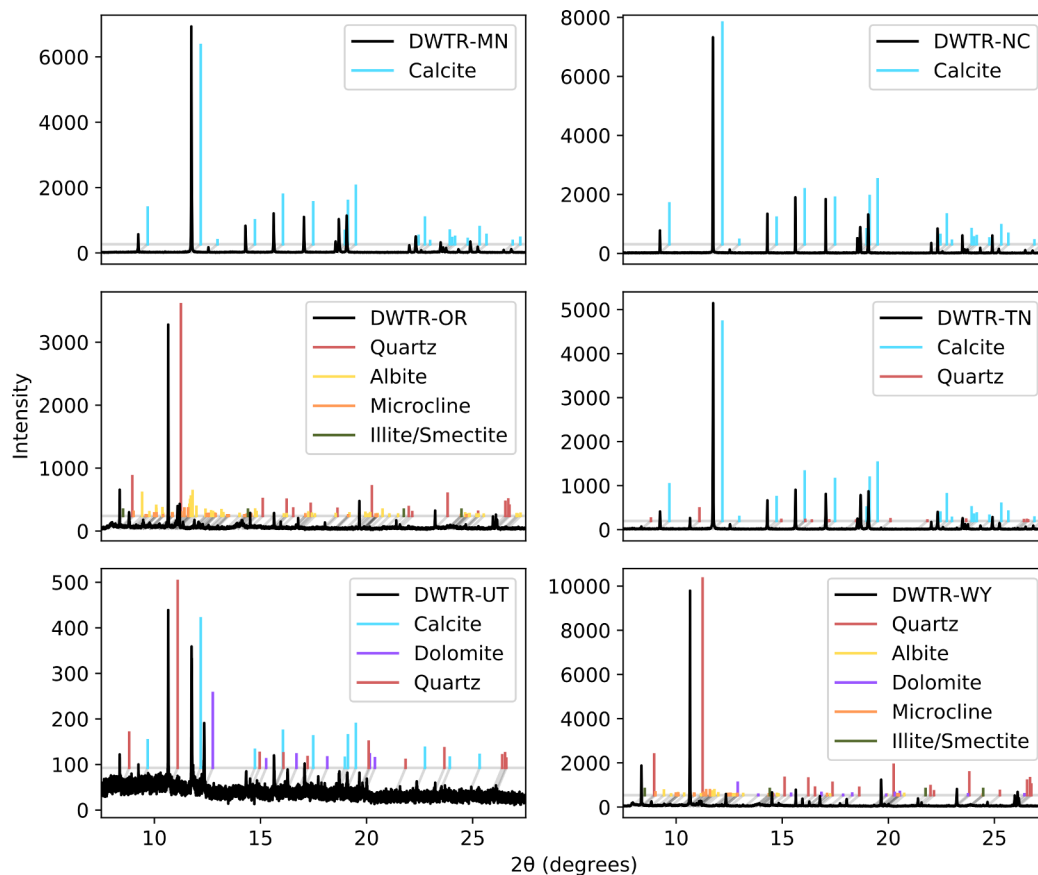


Fig. 7 Synchrotron-source X-ray diffraction patterns for the drinking water treatment residual samples, along with identified crystalline mineral phases. Peaks for calcite, quartz, albite, microcline, and dolomite were identified using JADE, as were the clay peaks attributable to either illite or smectite. Note that the intensities are not on the same scales; for instance, NC and WY samples show some especially intense diffraction patterns, while the UT sample has weak diffraction patterns, indicating a poorly crystalline sample.

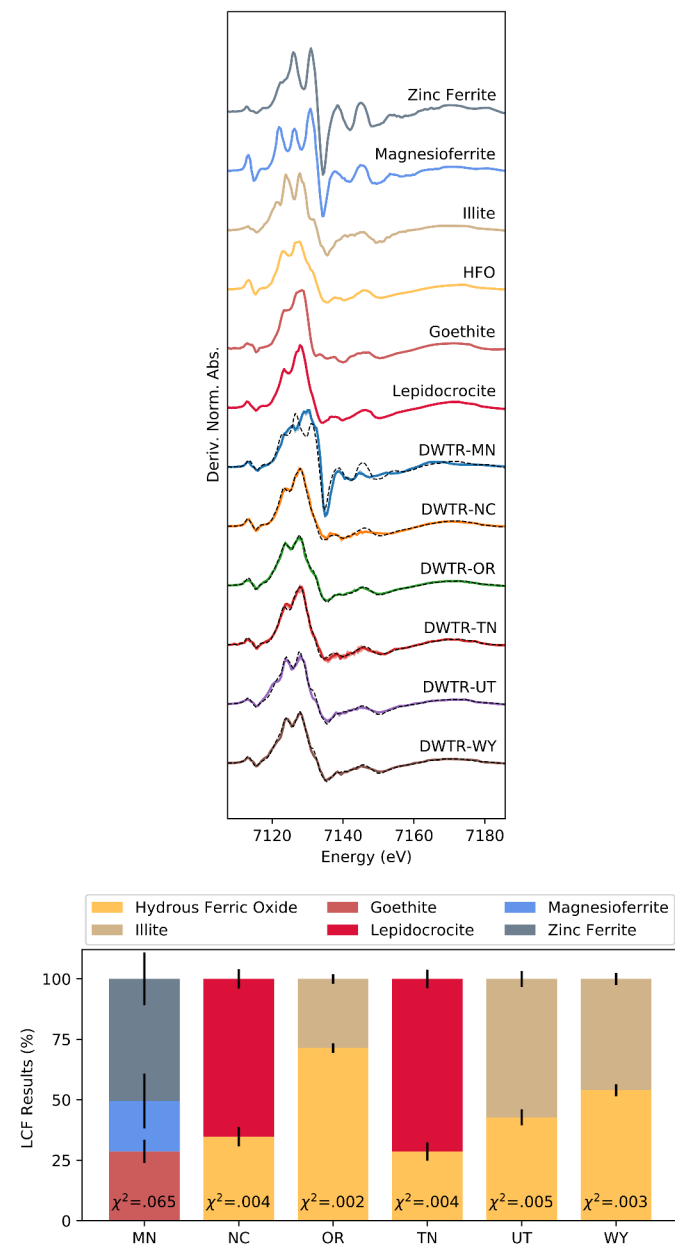


Fig. 8 Fe K-edge first-derivative XANES results for DWTRs. On the left, the spectra for the DWTRs and the standards employed in linear combination fitting (LCF) are shown. The merged spectra for the DWTRs are shown with a solid line, while the range in values from each scan is shown with a lighter shaded area. For most samples, the shaded region is too small to be seen (it may be observed near 7140 eV in the TN spectrum). The fit results using the standard spectra are shown with the dotted lines. On the right, the LCF results are shown as a bar chart, and  $\chi^2$  goodness-of-fit values are listed at the base of each bar.

structural iron in clay minerals rather than iron (oxy-)hydroxides. This aligns with previous findings highlighting complex nature of iron minerals in the environment, where ferric iron may be structurally incorporated into clays in significant fractions<sup>56</sup> or associated with a wide range of elements beyond what is found in simple iron oxides or oxy-hydroxides<sup>57</sup>.

NC and TN spectra are best reconstructed with HFO and lepidocrocite. For both samples, lepidocrocite accounts for the majority of the fit. Unlike the non-lime-based DWTRs, there is no spectroscopic (or crystallographic) evidence of iron associated with clays in these materials.

Finally, the MN sample is reconstructed using goethite, zinc ferrite<sup>27,28</sup>, and magnesioferrite<sup>27,28</sup>. The  $\chi^2$  value for this fit is much higher than in the other samples, indicating the imperfect nature of this result. However, this standard is able to account for the unusual features seen in the MN sample, including the shoulder and the oscillations. These features are not specific to magnesioferrite or zinc ferrite; in fact, they may be accounted for with a range of spinel ferrite materials not including magnetite. Spinel ferrite compounds adhere the general chemical formula of  $X^{2+}Fe_2O_4$ , where X is a divalent cation such as magnesium (forming magnesioferrite), copper (forming cuprospinel), manganese (forming jacobite), or ferrous iron (forming magnetite). In some spinel ferrites, ferric iron can at least partially occupy the tetrahedral sites more commonly occupied by the divalent cation, making an “inverse” spinel<sup>58</sup>. Other researchers using FDMNES ab initio XANES calculations identified the degree of inversion giving rise to the types of features seen in the MN sample’s XANES due to the contribution of tetrahedrally coordinated ferric iron to the spectra<sup>59,60</sup>.

Spinel ferrite chemical species may be precipitated when a solution containing both the divalent cation and ferric iron is mixed with a highly alkaline solution<sup>61</sup>. Generally, researchers synthesizing these minerals in the laboratory include an annealing and/or calcination step<sup>62</sup> to dehydrate and crystallize the material from precursor hydroxide minerals<sup>63</sup>; others have asserted that the spinel ferrite phase is precipitated at low temperatures, and the annealing step leads to longer-range crystal order<sup>64</sup>. Iron minerals may also transform into spinel ferrites, such as jacobite, provided a relatively high ratio of the divalent cation to the iron<sup>58,65</sup>. The magnesium and zinc spinel ferrite spectra best fit the MN spectrum, so they are used in the fit. Also plausible as a contributor is maghemite ( $\gamma\text{-Fe}_2\text{O}_3$ ), which possesses the spinel ferrite geometry with some octahedral site vacancies to balance the charge of the mineral<sup>58</sup>; maghemite forms through the oxidation of magnetite<sup>58</sup>, so magnetite coming from the groundwater’s source aquifer also presents a path for the presence of some of these spectral features.

### 3.5.2 Mn K-edge XAS.

Mn K-edge data for UT and TN are shown in Figure 9. Both DWTR samples are best reconstructed when manganese(II) carbonate makes up the plurality of the fit. For UT, a small fraction of the fit is allotted to  $Mn_3O_4$  and  $MnSiO_3$ <sup>31</sup>, which collectively have the effect of slightly muting the features of the  $MnCO_3$  spectrum rather than adding particularly distinct features. TN is more

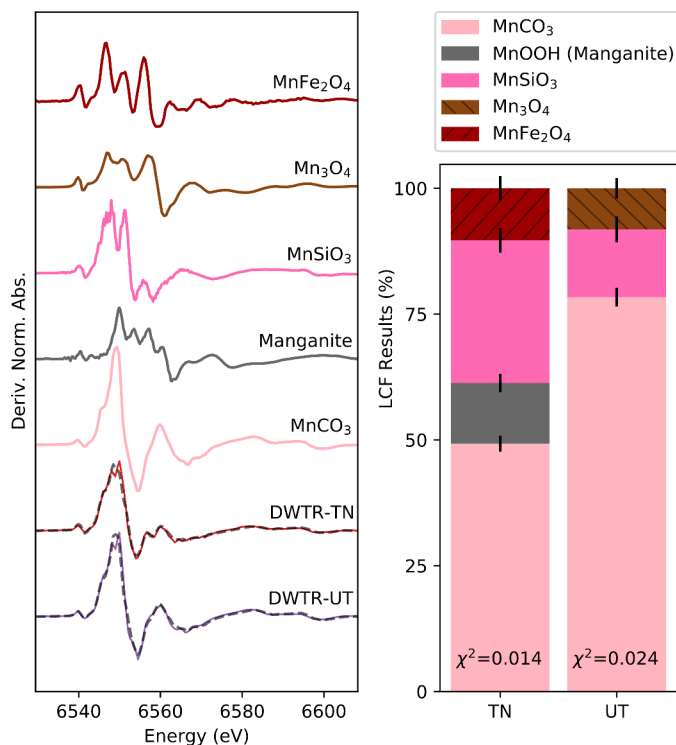


Fig. 9 Mn K-edge first-derivative XANES results for DWTRs. On the left, the linear combination fitting (LCF) results are shown with  $\chi^2$  goodness-of-fit values at the bottom of each bar. The right subplot shows the spectra for the DWTRs and the standards employed in LCF. As in Figure 8, the fit results using the standard spectra are shown with the dotted lines.

clearly different compared to the  $\text{MnCO}_3$  standard. The fit here uses manganite<sup>31</sup>,  $\text{MnSiO}_3$ <sup>31</sup>, and  $\text{MnFe}_2\text{O}_4$ <sup>27,28</sup>; both  $\text{MnSiO}_3$  and  $\text{MnFe}_2\text{O}_4$  help reconstruct the small feature near 6560 eV in the TN spectrum. Hausmannite, or  $\text{Mn}_3\text{O}_4$ , shows a feature in a similar location, though it does not help with the fit.  $\text{MnSiO}_3$  would not be expected to easily precipitate, and the TN sample lacks evidence for the presence of  $\text{MnFe}_2\text{O}_4$  in the Fe K-edge spectrum.

However, TN shows signs of oxidation over time, as shown in Figure 10. This progression shows a clear change towards spectral features consistent with hausmannite. On the other hand, UT has shown no signs of changes in speciation over time (Supplemental Figure ??).

Regardless, these results indicate that manganese is primarily – at least initially – in the reduced +2 oxidation state in these two DWTR samples. This has several implications. First, manganous species are more highly soluble than more oxidized forms of manganese, such as manganite ( $\text{MnO}(\text{OH})$ ) or manganese dioxide. In environmental applications, acidic conditions could dissolve the manganese in these DWTRs. On the other hand, placing these DWTRs in reducing conditions would not result in a sudden release of manganese. From the perspective of drinking water treatment, this does suggest that  $\text{Mn}^{2+}$  was not the target for oxidation by  $\text{KMnO}_4$  at the UT and TN DWTPs. Sulfide is also commonly removed by oxidation at DWTPs; the redox reactions between  $\text{HS}^-$  and  $\text{MnO}_4^-$  are shown in Equations 2, 3, and 4.

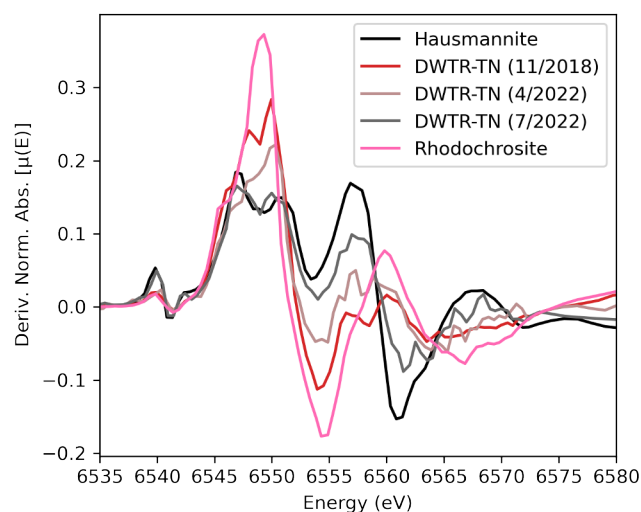
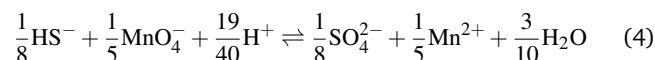
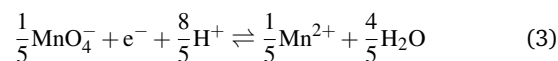
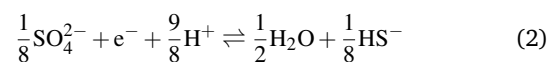


Fig. 10 Mn K-edge first-derivative XANES results for DWTR-TN over time. Rhodochrosite ( $\text{MnCO}_3$ ) and hausmannite ( $\text{Mn}_3\text{O}_4$ ) standards are shown for comparison. Initial scans show that the speciation of manganese in the TN sample is dominated by rhodochrosite. The spectrum increasingly matches that of hausmannite over time, suggesting the manganese in TN has become oxidized.



Manganese oxides are important controls on metal mobility in the environment<sup>66,67</sup>. Rhodochrosite ( $\text{MnCO}_3$ ), however, is not highly active in trace metal sorption processes like manganese oxide minerals<sup>68</sup>. Since  $\text{MnCO}_3$  represents a large fraction of the Mn speciation in the DWTRs that forms when using permanganate as an additive, it is unlikely that this solid phase would lead to significant metal immobilization. However, carbonates tend to dissolve at the sediment water interface as a result of the pH drop that results from organic matter degradation in presence of dissolved oxygen<sup>69</sup>. Therefore this store of Mn(II) is likely to oxidize and form manganese oxides<sup>70,71</sup> that are efficient at scavenging metals<sup>72</sup>.

## 4 Conclusions

Aluminum based drinking water treatment residuals are complex mixed materials that can drastically differ due to the composition of their additives. These additives may turn out to have more profound impacts on DWTRs sorption capacities than the solid phase formed by the use of aluminum salts. As we show in this report, they can result in large variations in the specific surface area of this material, as well as the formation of a few solid phases. Among the inorganic phases that are usually considered to control the sorption of metals, *i.e.*, Al, Fe, and Mn oxides-hydroxides,

these precipitates remain mostly amorphous; *i.e.*, they are not detected by high-resolution powder X-ray diffraction. The speciation of Fe and Mn can however be characterized by x-ray absorption spectroscopy, although some uncertainties remain when FeCl<sub>3</sub> and KMnO<sub>4</sub> are used. Interestingly, when KMnO<sub>4</sub> is used as an additive, most of the Mn is reduced to Mn(II) in the DWTR samples that we studied. Conversely, iron is present as Fe(III) species.

The use of lime as an additive profoundly impacts the composition of DWTRs, resulting in materials that contain significant carbonated fractions. The dissolution of this fraction will then provide a buffering mechanism in environmental applications where DWTRs are expected to be exposed to acidic solutions, hence limiting metal desorption. In addition, the formation of MnCO<sub>3</sub> will provide a reservoir for the formation of MnO<sub>x</sub> in presence of dissolved O<sub>2</sub> that should lead to an effective scavenging of metals. For non-lime-based DWTRs, some broad similarities are observed across their characterizations. Elemental and surface area analyses highlight the impact of activated carbon as an additive, particularly in the UT sample. Even as a spent waste material, the high surface area of DWTR-UT makes it an attractive candidate for sorbing and immobilizing metal and other pollutants. Lastly, the significant organic matter content as shown by CHNS analyses, especially in DWTRs without a lime additive, may also promote favorable conditions for metal binding.

## Author Contributions

**Samuel Wallace:** Investigation, formal analysis, writing - original draft, visualization, data curation. **Yuchi Zhang:** Investigation (BET). **Lang Zhou:** Investigation (sample prep/analysis), data curation. **Qing Ma:** Investigation (x-ray absorption spectroscopy). **William Guise:** Investigation (high-resolution powder x-ray diffraction). **Nancy Denslow:** Supervision, funding acquisition, writing - review and editing. **Jean-Claude Bonzongo:** Supervision, funding acquisition, writing - review and editing. **Jean-François Gaillard:** Conceptualization, validation, funding acquisition, supervision, writing - review and editing.

## Conflicts of interest

There are no conflicts to declare.

## Electronic supplementary information

The raw data for this article can be found at: <https://github.com/jfgaillard/A1-DWTR-Characterization-data>

## Acknowledgements

Funding for this research was provided by the US Department of Defense's Strategic Environmental Research and Development Program (project ER18-C4-1428) and the Institute for Sustainability and Energy at Northwestern's Cluster Fellowship. This work made use of the IMSERC X-RAY facility at Northwestern University, which has received support from the Soft and Hybrid Nanotechnology Experimental (SHyNE) Resource (NSF ECCS-2025633) and Northwestern University; and the Jerome B. Cohen X-Ray Diffraction Facility, supported by the MRSEC program of the National Science Foundation (DMR-1720139) at the Materi-

als Research Center of Northwestern University and the Soft and Hybrid Nanotechnology Experimental (SHyNE) Resource (NSF ECCS-2025633). The REACT Facility of the Northwestern University Center for Catalysis and Surface Science is supported by a grant from the DOE (DE-SC0001329). Portions of this work were performed at the DuPont-Northwestern-Dow Collaborative Access Team (DND-CAT) located at Sector 5 of the Advanced Photon Source (APS). DND-CAT is supported by Northwestern University, The Dow Chemical Company, and DuPont de Nemours, Inc. This research used resources of the Advanced Photon Source, a U.S. Department of Energy (DOE) Office of Science User Facility operated for the DOE Office of Science by Argonne National Laboratory under Contract No. DE-AC02-06CH11357.

## Notes and references

- 1 J. A. Ippolito, K. A. Barbarick and H. A. Elliott, *Journal of Environmental Quality*, 2011, **40**, 1–12.
- 2 J. C. Crittenden, R. R. Trussell, D. W. Hand, K. J. Howe and G. Tchobanoglous, *Water Treatment: Principles and Design*, John Wiley & Sons, 2012.
- 3 U.S. Environmental Protection Agency, *Drinking Water Treatment Plant Residuals Management Technical Report*, 2011.
- 4 U.S. Environmental Protection Agency, *Drinking Water Treatment Residual Injection Wells - Technical Recommendations*, 2006.
- 5 Y. Q. Zhao, R. B. Liu, O. W. Awe, Y. Yang and C. Shen, *Chemical Engineering Journal*, 2018, **353**, 717–726.
- 6 Y. H. Ai, S. Lee and J. Lee, *Science of the Total Environment*, 2020, **706**, 135756.
- 7 L. Zhou, S. M. Wallace, K. J. Kroll, N. D. Denslow, J. F. Gailard, P. Meyer and J. C. J. Bonzongo, *Environmental Toxicology and Chemistry*, 2021, **40**, 2005–2014.
- 8 T. Turner, R. Wheeler, A. Stone and I. Oliver, *Water Air and Soil Pollution*, 2019, **230**, 1–30.
- 9 J. Mallevalle, A. Bruchet and F. Fiessinger, *Journal American Water Works Association*, 1984, **76**, 87–93.
- 10 M. Wolowiec, M. Komorowska-Kaufman, A. Pruss, G. Rzepa and T. Bajda, *Minerals*, 2019, **9**, 487.
- 11 D. Sarkar, K. C. Makris, V. Vandanapu and R. Datta, *Environmental Pollution*, 2007, **146**, 414–419.
- 12 K. C. Makris, D. Sarkar, J. G. Parsons, R. Datta and J. L. Gardea-Torresdey, *Journal of Colloid and Interface Science*, 2007, **311**, 544–550.
- 13 S. Agyin-Birikorang, O. O. Oladeji, G. A. O'Connor, T. A. Obreza and J. C. Capece, *Journal of Environmental Quality*, 2009, **38**, 1076–1085.
- 14 J. A. Ippolito, K. A. Barbarick, D. M. Heil, J. P. Chandler and E. F. Redente, *Journal of Environmental Quality*, 2003, **32**, 1857–1864.
- 15 K. D. Quinones, A. Hovsepian, A. Oppong-Anane and J. C. J. Bonzongo, *Journal of Hazardous Materials*, 2016, **307**, 184–192.
- 16 A. Hovsepian and J. C. J. Bonzongo, *Journal of Hazardous Materials*, 2009, **164**, 73–80.

- 17 L. Zhou, S. M. Wallace, N. D. Denslow, J. F. Gaillard, P. Meyer and J. C. J. Bonzongo, *Environmental Toxicology and Chemistry*, 2021, **40**, 1194–1203.
- 18 S. Brunauer, P. H. Emmett and E. Teller, *Journal of the American Chemical Society*, 1938, **60**, 309–319.
- 19 E. P. Barrett, L. G. Joyner and P. P. Halenda, *Journal of the American Chemical Society*, 1951, **73**, 373–380.
- 20 G. Halsey, *Journal of Chemical Physics*, 1948, **16**, 931–937.
- 21 S. C. Phillips, J. E. Johnson, E. Miranda and C. Disenhof, *Limnology and Oceanography-Methods*, 2011, **9**, 194–203.
- 22 Materials Data, *Jade Pro*, 2020.
- 23 S. Gates-Rector and T. Blanton, *Powder Diffraction*, 2019, **34**, 352–360.
- 24 R. T. Downs and M. Hall-Wallace, *American Mineralogist*, 2003, **88**, 247–250.
- 25 M. Xie, M. A. Alsina, J. Yuen, A. I. Packman and J.-F. Gaillard, *Journal of Hazardous Materials*, 2019, **364**, 300–308.
- 26 S. Fakra, *Xas Databases*, 2010, <http://xraysweb.lbl.gov/uxas/databases/overview.htm>.
- 27 M. Tanifuji, A. Matsuda and H. Yoshikawa, 2019 8th International Congress on Advanced Applied Informatics (IIAI-AAI), 2019, pp. 1021–1022.
- 28 M. Ishii, H. Nagao, K. Tanabe, A. Matsuda and H. Yoshikawa, *MDR XAFS DB*, 2021, Materials Data Repository, National Institute for Materials Science.
- 29 I. Saratovsky, P. G. Wightman, P. A. Pasten, J.-F. Gaillard and K. R. Poeppelmeier, *Journal of the American Chemical Society*, 2006, **128**, 11188–11198.
- 30 B. Ravel and M. Newville, *Journal of Synchrotron Radiation*, 2005, **12**, 537–541.
- 31 A. Manceau, M. A. Marcus and S. Grangeon, *American Mineralogist*, 2012, **97**, 816–827.
- 32 M. A. Alsina, S. M. Wallace, M. Desmau and J.-F. Gaillard, XAFS 2021 Virtual, 2021.
- 33 T. Kluyver, B. Ragan-Kelley, F. Perez, B. Granger, M. Bussonnier, J. Frederic, K. Kelley, J. Hamrick, J. Grout, S. Corlay, P. Ivanov, D. Avila, S. Abdalla, C. Willing and T. Jupyter Dev, *Positioning and Power in Academic Publishing: Players, Agents and Agendas*, 2016, 87–90.
- 34 P. Virtanen, R. Gommers, T. E. Oliphant, M. Haberland, T. Reddy, D. Cournapeau, E. Burovski, P. Peterson, W. Weckesser, J. Bright, S. J. van der Walt, M. Brett, J. Wilson, K. J. Millman, N. Mayorov, A. R. J. Nelson, E. Jones, R. Kern, E. Larson, C. J. Carey, I. Polat, Y. Feng, E. W. Moore, J. VanderPlas, D. Laxalde, J. Perktold, R. Cimrman, I. Henriksen, E. A. Quintero, C. R. Harris, A. M. Archibald, A. N. H. Ribeiro, F. Pedregosa, P. van Mulbregt and C. SciPy, *Nature Methods*, 2020, **17**, 261–272.
- 35 F. Pedregosa, G. Varoquaux, A. Gramfort, V. Michel, B. Thirion, O. Grisel, M. Blondel, P. Prettenhofer, R. Weiss, V. Dubourg, J. Vanderplas, A. Passos, D. Cournapeau, M. Brucher, M. Perrot and E. Duchesnay, *Journal of Machine Learning Research*, 2011, **12**, 2825–2830.
- 36 C. R. Harris, K. J. Millman, S. J. van der Walt, R. Gommers, P. Virtanen, D. Cournapeau, E. Wieser, J. Taylor, S. Berg, N. J. Smith, R. Kern, M. Picus, S. Hoyer, M. H. van Kerkwijk, M. Brett, A. Haldane, J. F. del Rio, M. Wiebe, P. Peterson, P. Gerard-Marchant, K. Sheppard, T. Reddy, W. Weckesser, H. Abbasi, C. Gohlke and T. E. Oliphant, *Nature*, 2020, **585**, 357–362.
- 37 S. M. Wallace, M. A. Alsina and J. F. Gaillard, *Journal of Synchrotron Radiation*, 2021, **28**, 1178–1183.
- 38 J.-F. Gaillard, S. M. Webb and J. P. Quintana, *Journal of Synchrotron Radiation*, 2001, **8**, 928–930.
- 39 C. Da Silva-Cadoux, L. Zanella and J. F. Gaillard, *Journal of Analytical Atomic Spectrometry*, 2012, **27**, 957–965.
- 40 S. M. Webb and J.-F. Gaillard, *Aquatic Geochemistry*, 2015, **21**, 295–312.
- 41 M. Newville, T. Stensitzki, D. B. Allen, M. Rawlik, A. Ingargiola and A. Nelson, *Astrophysics Source Code Library*, 2016.
- 42 R. Pallasser, B. Minasny and A. B. McBratney, *PeerJ*, 2013, **1**, e6.
- 43 M. Kristl, M. Mursec, V. Sustar and J. Kristl, *Journal of Thermal Analysis and Calorimetry*, 2016, **123**, 2139–2147.
- 44 D. Tokarski, M. Wiesmeier, H. D. Weissmannova, K. Kalbitz, M. S. Demyan, J. Kucerik and C. Siewert, *Geoderma*, 2020, **362**, 114124.
- 45 S. J. Gregg and J. P. Saenz, *Journal of Applied Chemistry*, 1966, **16**, 300–+.
- 46 S. A. Craik, M. R. Gray, S. E. Hrudey and P. M. Fedorak, *Environmental Technology*, 1991, **12**, 489–496.
- 47 D. Dittmann, U. Braun, M. Jekel and A. S. Ruhl, *Journal of Environmental Chemical Engineering*, 2018, **6**, 2222–2231.
- 48 E. Z. Silvero, J. G. Albiol, E. M. Diaz-Canales, M. J. V. Vaguer and M. P. Gomez-Tena, *Minerals*, 2020, **10**, 824.
- 49 J. R. Degnan, B. D. Lindsey, J. P. Levitt and Z. Szabo, *Science of the Total Environment*, 2020, **723**, 137835.
- 50 E. P. Bertin, *Principles and Practice of X-Ray Spectrometric Analysis*, Plenum Press, New York, N.Y., 2nd edn, 1975.
- 51 A. Guinier, *X-ray diffraction in crystals, imperfect crystals, and amorphous bodies*, Courier Corporation, 1994.
- 52 R. Hardy and M. Tucker, in *Techniques in Sedimentology*, Blackwell Scientific Publications, 1988, ch. X-ray powder diffraction of sediments, pp. 191–228.
- 53 J. Berkowitz, M. A. Anderson and R. C. Graham, *Water Research*, 2005, **39**, 3918–3928.
- 54 A. C. Kuster, A. T. Kuster and B. J. Huser, *Journal of Environmental Management*, 2020, **261**, 110195.
- 55 A. C. Kuster, B. J. Huser, S. Padungthon, R. Junggoth and A. T. Kuster, *Water*, 2021, **13**, 2465.
- 56 J. S. Yan, N. Sharma, E. D. Flynn, D. E. Giammar, G. E. Schwartz, S. C. Brooks, P. Weisenhorn, K. M. Kemner, E. J. O’Loughlin, D. I. Kaplan and J. G. Catalano, *Geochimica Et Cosmochimica Acta*, 2022, **317**, 234–254.
- 57 D. Perret, J. F. Gaillard, J. Dominik and O. Atteia, *Environmental Science and Technology*, 2000, **34**, 3540–3546.
- 58 U. Schwertmann and R. M. Cornell, *Iron Oxides in the Laboratory: Preparation and Characterization*, John Wiley & Sons,

- 2008.
- 59 J. Jutimoosik, P. Kidkhunthod, T. Bongkarn and R. Yimnirun, *Ferroelectrics*, 2019, **552**, 177–185.
- 60 J. Jutimoosik, P. Kidkhunthod, T. Bongkarn and R. Yimnirun, *Radiation Physics and Chemistry*, 2021, **188**, 109628.
- 61 T. Tatarchuk, M. Bououdina, J. J. Vijaya and L. J. Kennedy, 4th International Research and Practice Conference on Nanotechnology and Nanomaterials (NANO), 2017, pp. 305–325.
- 62 P. S. A. Kumar, J. J. Shrotri, S. D. Kulkarni, C. E. Deshpande and S. K. Date, *Materials Letters*, 1996, **27**, 293–296.
- 63 P. Ren, J. X. Zhang and H. Y. Deng, *Journal of Wuhan University of Technology-Materials Science Edition*, 2009, **24**, 927–930.
- 64 Z. X. Tang, C. M. Sorensen, K. J. Klabunde and G. C. Hadjipanayis, *Journal of Colloid and Interface Science*, 1991, **146**, 38–52.
- 65 R. M. Cornell and R. Giovanoli, *Clays and Clay Minerals*, 1987, **35**, 11–20.
- 66 N. Takematsu, *Journal of the Oceanographical Society of Japan*, 1979, **35**, 36–42.
- 67 E. A. Jenne, in *Controls on Mn, Fe, Co, Ni, Cu, and Zn Concentrations in Soils and Water: The Significant Role of Hydrous Mn and Fe Oxides*, American Chemical Society, 1968, vol. 73, book section 21, pp. 337–387.
- 68 S. Namgung and G. Lee, *Environmental Science and Technology*, 2021, **55**, 14436–14444.
- 69 R. A. Jahnke, D. B. Craven and J.-F. Gaillard, *Geochimica et Cosmochimica Acta*, 1994, **58**, 2799–2809.
- 70 C. Rabouille and J.-F. Gaillard, *Geochimica et Cosmochimica Acta*, 1991, **55**, 2511–2525.
- 71 P. VanCappellen and J.-F. Gaillard, *Reactive Transport in Porous Media*, 1996, pp. 335–376.
- 72 C. P. Lienemann, M. Taillefert, D. Perret and J.-F. Gaillard, *Geochimica et Cosmochimica Acta*, 1997, **61**, 1437–1446.